We are IntechOpen, the world's leading publisher of Open Access books Built by scientists, for scientists

4,800
Open access books available

122,000
International authors and editors

135M
Downloads

Our authors are among the

154
Countries delivered to

TOP 1%
most cited scientists

12.2%
Contributors from top 500 universities

CLARIVATE ANALYTICS BOOK CITATION INDEX INDEXED

WEB OF SCIENCE™

Selection of our books indexed in the Book Citation Index in Web of Science™ Core Collection (BKCI)

Interested in publishing with us?
Contact book.department@intechopen.com

Numbers displayed above are based on latest data collected.
For more information visit www.intechopen.com

Chapter 12

Impact of Fluid Flow on Free Radical Polymerization in a Batch Reactor

Gerardo M. Pineda-Torres, Cecilia Durán-Valencia, Fernando Barragán-Aroche and Simon López-Ramírez

Additional information is available at the end of the chapter

http://dx.doi.org/10.5772/64156

Abstract

In this work, the mixing process on a batch reactor is analyzed for the thermal synthesis of poly(acrylamide-co-sodium 2-acrylamide-2-methylpropane sulfonate) initiated by ammonium persulfate. The analysis is achieved by using tracer technology and computational fluid dynamics (CFD). ANSYS Fluent® software is used for numerical simulations. By studying the mixing time in the reactor, the injection point and the stirring speed are determined so that the kinetics of copolymerization is improved.

The kinetics of copolymerization is studied qualitatively based on the solution of the inverse rheokinetic problem. The progress of co-polymerization was registered with a Rheometer Anton Paar MCR 301®. The copolymers synthetized were characterized by capillary viscometry, infrared spectroscopy, calorimetry, and rheology.

Keywords: CFD, rheokinetics, rheology, batch reactor, polymerization

1. Introduction

Modeling of chemical reactors attempts to solve both conservation (mass, energy, and momentum) and chemical kinetics equations [1]. The complexity of the mathematics involved can be drastically reduced by considering that convection dominates the diffusion, by assuming a unidimensional scenario or by simplifying the momentum transport equations [2]. Nevertheless, these assumptions may oversimplify the mathematical model by neglecting mixing problems. Mixing plays a fundamental role in reaction engineering. For instance, the

kinetics, the molecular weight, and the composition of polymers can be altered due to local concentration gradients as a consequence of bad mixing [3].

In this study, a batch chemical reactor is analyzed. This type of reactor is defined as a closed and spatially uniform system where the chemical species are transformed only as a function of time. The transformation of chemical species can be quantified by following any physicochemical property associated with either reagents or products. During free radical polymerizations, the viscosity of the medium increases dramatically while products are formed [4]. The kinetics of polymerization can be followed from the change of viscosity.

Rapid computational development has made the numerical analysis of phenomena associated with stirred tanks easier [5]. For example, through CFD, Patel [6] studied the mixing process on a continuous stirred tank reactor and how the thermal polymerization of styrene is affected.

Computational analysis in stirred reactors has to consider at least two models: one for turbulence and the other for stirring. The turbulence model describes the random and chaotic movement of a fluid [7], while the stirring model describes the displacement of the fluid as a consequence of the local movement of mechanical parts.

The study of batch reactors with a tracer is the basis for understanding flow behavior [8]. Tracer evolution curves allow to identify regions with turbulence, dead zones, recirculation cycles, closed circuits, or even to determine the mixing time of the reactor [9, 10].

In this work, a tracer test was used to validate a mathematical model. The mixing process was analyzed by using both the experimental and simulated behavior of the tracer. The experimental kinetics of polymerization was obtained by a multiparametric nonlinear regression of viscosity-time data.

2. Problem definition

The uses of polyacrylamide have been extended to different applications in the oil industry, such as water conformance, fracking, and enhanced oil recovery (EOR) processes.

In EOR applications, acrylamide (AAm) polymers are dispersed in water to increase their viscosity. However, at high temperatures the viscosity of AAm polymer decreases due to hydrolysis [11]. This can be mitigated by using co-monomers such as sodium 2-acrylamido-2-methylpropane sulfonate (AMPSNa) [12]. This sodium sulfonate monomer is well known because it confers stability to the polymer against divalent cations and high temperatures (above 90°C). In view of the benefits, it is necessary to develop a process for the synthesis of the AAm-AMPSNa copolymer that guarantees product quality and synthesis reproducibility in order to properly design the polymer. The next sections will be focused on studying the relation between the mixing time and the mixing process during the synthesis of copolymer in a batch reactor.

http://dx.doi.org/10.5772/64156

3. Rheokinetics and inverse problem

The kinetics of polymerization was analyzed through the evolution of rheological behavior of the reactive system. Rheology has entered into science fields, such as biology and polymer science [13]. Historically, polymer science and rheology converge in what is known as rheokinetics. This field was created more than 30 years ago to have a better understanding of the phenomenological nature of polymerizations.

There are two main problems related to rheokinetics: the direct and inverse problems. The inverse problem, which is the principal focus of this work, deals with the determination of kinetic parameters given by the experimental data of viscosity-time curves. Equation (4) reproduces the viscosity-time curve behavior (rheokinetic model) and it was obtained from Eqs. (1–3). This equation assumes a linear free radical polymerization and it does not consider mass and energy transport effects. Equations (1) through (4) are deeply analyzed by Malkin, see [14].

$$\eta = Kx^b \bar{N}^a \tag{1}$$

$$x = 1 - exp\left(-\frac{k_p k_d^{1/2} f^{1/2}}{k_t^{1/2}} [I]_o^{1/2} t \right) \tag{2}$$

$$\bar{N} = \frac{[M]_o}{[I]_o} x\left(1 - exp\left(-k_d t\right)\right) \tag{3}$$

$$\eta = K[M]_o^{\ a}[I]_o^{\ -a}\left[1 - exp\left(-\frac{2f^{1/2}}{k_d^{1/2}} \frac{k_p}{k_t^{1/2}} [I]_o^{\ 1/2}\left[1 - exp\left(-k_d t\right)\right] \right)\right]^{a+b} \tag{4}$$

where η is the viscosity, t is the reaction time, $\bar{N}$ is the polymerization degree, x is the conversion, $[M]_o$ is the initial monomer concentration, $[I]_o$ is the initial initiator concentration, K, a, b, and f are system parameters and k_p, k_t, k_d are the rate constants of propagation, termination, and initiation, respectively.

The ratio $k_p / k_t^{1/2}$ is estimated as proposed by **Figure 1**. To guarantee the quality of the adjustment, k_d must be a number between 0.01 and 1 [4]. To know which process dominates the polymerization, the magnitude of $k_p / k_t^{1/2}$ is used an indicator. If the ratio is $k_p / k_t^{1/2} \gg 1$, the propagation of live chains dominates; on the contrary, when $k_p / k_t^{1/2} \ll 1$, the termination of macro radicals dominates.

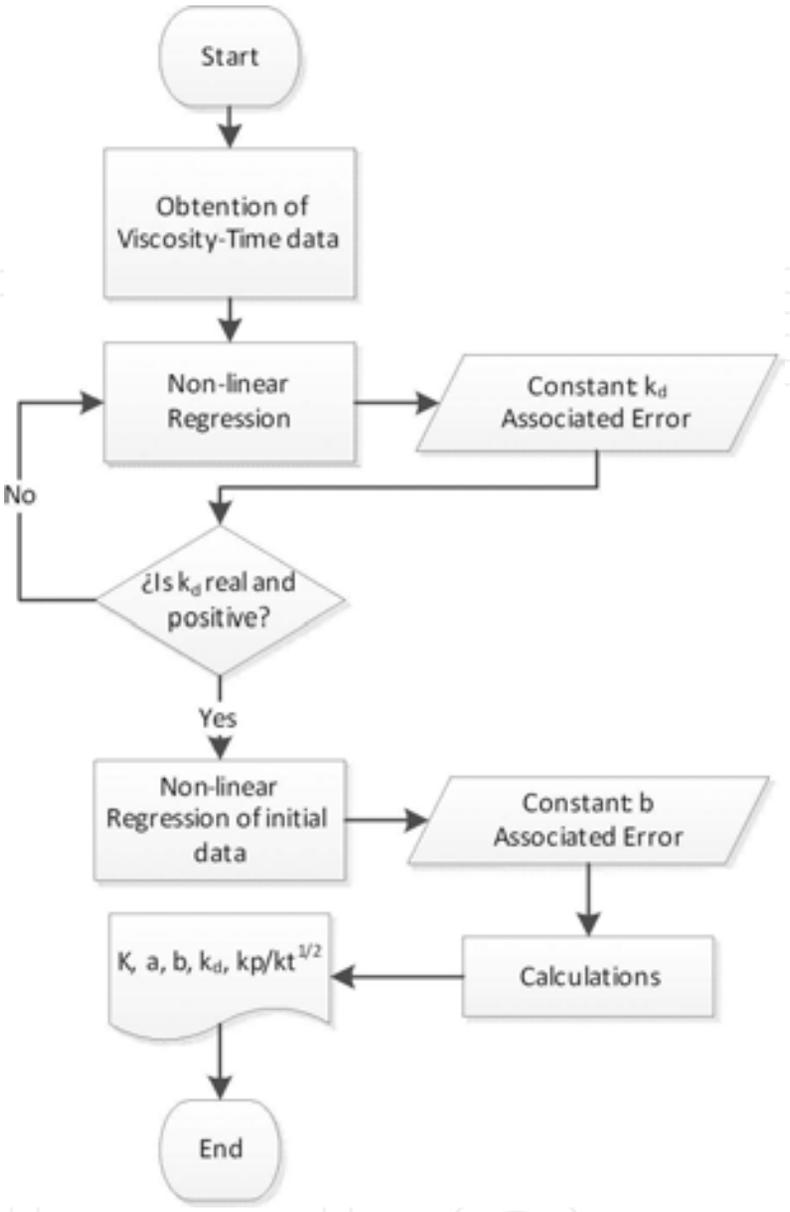

Figure 1. Estimation of $k_p / k_t^{1/2}$ from viscosity-time experimental data.

4. Computational fluid dynamics (CFD)

CFD is concerned with the numerical solution of the following partial differential equations that express the conservation principles of mass, energy, and momentum transport (5–7) [2].

$$\frac{\partial x_A}{\partial t} + \left(\nabla \cdot \mathbf{v} x_A\right) - \left(\nabla \cdot \nabla D_{AB} x_A\right) - R_A + S_A = 0 \tag{5}$$

$$\frac{\partial \rho C_p T}{\partial t} + \left(\nabla \cdot \mathbf{v} \rho C_p T\right) - \left(\nabla \cdot \nabla k \rho C_p T\right) - q_R + q_I = 0 \tag{6}$$

$$\frac{\partial \rho \mathbf{v}}{\partial t} + \left[\nabla \cdot \rho \mathbf{v}\mathbf{v}\right] - \mathbf{g}\rho + \nabla P + \left[\nabla \cdot \boldsymbol{\tau}\right] = \mathbf{0} \tag{7}$$

where x_A is the concentration of "A" species, T is the temperature, $\mathbf{v}$ is the velocity, ρ is the density, C_p is the heat capacity, D_{AB} is the diffusion coefficient, k is the thermal conductivity, $\mathbf{g}$ is the gravity, P is the pressure, $\boldsymbol{\tau}$ is the stress tensor, R_A *y* q_R are terms associated with the chemical reaction, S_A *y* q_I are source terms and $\nabla = \frac{\partial}{\partial x_i}$.

Equations (5–7) are supported in two assumptions. The first one is the conservation principle which states that mass, energy, and momentum are transformed without creating or destroying themselves and the second one is the continuum hypothesis which considers continuity of its physical properties [15].

When simplifying Eq. (7) by considering a fluid of constant density and viscosity and a linear relation between the shear rate and the shear stress, the Navier-Stokes equations can be obtained Eq. (8):

$$\rho \frac{\mathrm{D}\mathbf{v}}{\mathrm{Dt}} - \mathbf{g}\rho + \nabla P - \mu\left[\nabla \cdot \nabla \mathbf{v}\right] = \mathbf{0} \tag{8}$$

Navier-Stokes equations are the basis of CFD and its numerical solution is fundamental to understand and describe the phenomena of fluid flow.

A CFD simulation is limited by the data processing rates and storing capacity. Nevertheless, improvements of computers capacity have stimulated the growth and diversification of CFD applications [16]. Nowadays, there are several CFD software tools as COMSOL® and Fluent®.

5. Fluent® simulation

A typical simulation comprises the formulation of the problem, physical assumptions to simplify the mathematical model, the numerical solution of the conservation equations, data processing, and the discussion of results. The mathematical models, initial conditions, and other adjustments can be implemented through Fluent® software.

In **Figure 2**, there are at least two critical stages: convergence of the numerical solution and validation of the mathematical model.

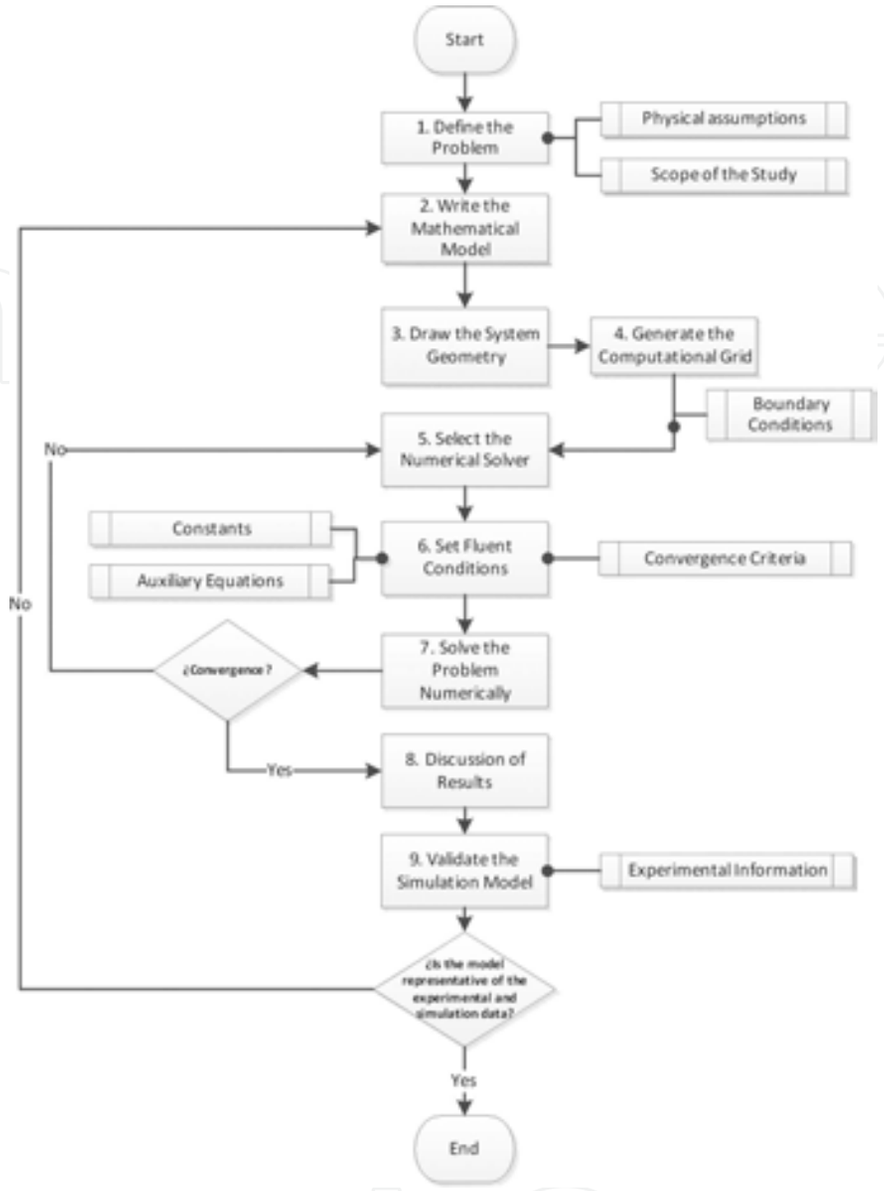

Figure 2. Development of a Fluent® simulation.

6. Turbulence and RANS equations

Turbulence is described as a random and chaotic movement of a fluid. Mathematically, a turbulence model is a nonlinear system in which a minimum modification on its boundary conditions produces severe alterations in the global behavior of the system [17]. Ranade proposes three approaches to model turbulence in fluids: statistical, deterministic, and structural [2]. Reynolds-average Navier-Stokes (RANS) equations are part of the statistical approximation in which turbulence is described as a combination of average variables (θ_i) and fluctuations θ_f [18]:

$$\theta_i = \bar{\theta}_i + \theta_f \tag{9}$$

Semi-empirical k-ϵ is a turbulence model commonly used in stirred tanks. The model assumes complete turbulence and neglects molecular viscosity effects. k-ϵ is part of the RANS equations and it is composed by a two-equation system with two parameters to solve: k (turbulence kinetic energy) and ϵ (turbulence dissipation rate). Standard k-ϵ was the first model; RNG (renormalization group theory) and realizable models were developed from subsequent modifications [19]. In contrast to standard k-ϵ, RNG improves flow with eddies and it adds a term to the ϵ equation ($R\epsilon$).

$$\frac{\partial(\rho k)}{\partial t} + \nabla \cdot \mathbf{v}(\rho k) = \nabla \cdot \left[\propto_k \mu_{eff} \nabla k \right] + G_k + G_b - \rho\epsilon - Y_M + S_k \tag{10}$$

$$\frac{\partial(\rho \epsilon)}{\partial t} + \nabla \cdot \mathbf{v}(\rho \epsilon) = \nabla \cdot \left[\propto_k \mu_{eff} \nabla \epsilon \right] + C_{1\epsilon} \frac{\epsilon}{k}(G_k + C_{3\epsilon} G_b) - C_{2\epsilon} \rho \frac{\epsilon^2}{k} - R_\epsilon + S_\epsilon \tag{11}$$

Realizable k-ϵ has a superior performance for rotational flows and for boundary layers under adverse conditions like high-pressure gradients, separation, and recirculation [18].

$$\frac{\partial(\rho k)}{\partial t} + \nabla \cdot \mathbf{v}(\rho k) = \nabla \cdot \left[\left(\mu + \frac{\mu_t}{\sigma_k} \right) \nabla k \right] + G_k + G_b - \rho\epsilon - Y_M + S_k \tag{12}$$

$$\frac{\partial(\rho \epsilon)}{\partial t} + \nabla \cdot \mathbf{v}(\rho \epsilon) = \nabla \cdot \left[\left(\mu + \frac{\mu_t}{\sigma_\epsilon} \right) \nabla \epsilon \right] + \rho C_1 S_\epsilon - \rho C_2 \frac{\epsilon^2}{k + \sqrt{\nu\epsilon}} + C_{1\epsilon} \frac{\epsilon}{k} C_{3\epsilon} G_b + S_\epsilon \tag{13}$$

$$C_1 = \max\left(0.43, \frac{\eta}{\eta + 5} \right) \tag{14}$$

$$S = \sqrt{2\mathbf{S_{ij}}\mathbf{S_{ij}}} \tag{15}$$

$$\eta = S \frac{k}{\epsilon} \tag{16}$$

where G_k is the generation of "k" by velocity gradients and G_b by buoyancy, S_k and S are source terms, C_2 and C_1 are constants, and σ_k and σ_k are σ are the turbulent Prandtl numbers for k and ϵ, respectively. Turbulent viscosity (μ_t) is calculated as indicated by Eq. (17):

$$\mu_t = \rho C_\mu \frac{k^2}{\epsilon} \tag{17}$$

In contrast to RNG, realizable model uses a variable C_μ that satisfies the "realizability" through Schwarz shear rate inequality and by making the normal stress tensor positive.

$$C_\mu = \frac{1}{4.04 + \frac{\sqrt{6cos\phi kU^*}}{\epsilon}} \tag{18}$$

U^* is calculated by Eq. (19), where $\overline{\mathbf{\Omega_{ij}}}$ is the rotation average speed tensor on a rotating reference frame with angular velocity $\boldsymbol{\omega}_\mathbf{k}$:

$$U^* = \sqrt{\mathbf{S_{ij}S_{ij}} + \widetilde{\mathbf{\Omega}}_\mathbf{ij}\widetilde{\mathbf{\Omega}}_\mathbf{ij}} \tag{19}$$

$$\widetilde{\mathbf{\Omega}}_\mathbf{ij} = \mathbf{\Omega_{ij}} - \mathbf{2}\boldsymbol{\epsilon}_\mathbf{ijk}\boldsymbol{\omega}_\mathbf{k} \tag{20}$$

$$\mathbf{\Omega_{ij}} = \overline{\mathbf{\Omega}_{IJ}} - \boldsymbol{\epsilon}_\mathbf{ijk}\boldsymbol{\omega}_\mathbf{k} \tag{21}$$

7. Stirring model

CFD simulation of moving parts, e.g. impellers and turbines, requires approximations that consider the displacement and rotation of mechanical parts on a computational grid. The most used models for stirred tanks are the moving reference frame (MRF) and the sliding mesh (SM). In contrast to MRF, SM requires more computational resources and its convergence time is higher.

MRF is defined by a rotational and a stationary region. The equations are solved on a reference frame that rotates with the impeller and the problem is solved on a stationary grid [20]. When the momentum equation is solved, an additional acceleration term is incorporated in the velocity vector formulation as relative Eq. (22) or absolute Eq. (23).

$$\frac{\partial \rho \mathbf{v_r}}{\partial t} + \left[\nabla \cdot \rho \mathbf{v_r v_r}\right] + \rho\left[2\mathbf{w} \times \mathbf{v_r} + \mathbf{w} \times \mathbf{w} \times \mathbf{r}\right] - \mathbf{g}\rho + \nabla P + \left[\nabla \cdot \boldsymbol{\tau}\right] = 0 \tag{22}$$

$$\frac{\partial \rho \mathbf{v}}{\partial t} + \left[\nabla \cdot \rho \mathbf{v_r v}\right] + \rho\left[\mathbf{w} \times \mathbf{v}\right] - \mathbf{g}\rho + \nabla P + \left[\nabla \cdot \boldsymbol{\tau}_\mathbf{r}\right] = \mathbf{0} \tag{23}$$

http://dx.doi.org/10.5772/64156

The term $\rho[\mathbf{2w} \times \mathbf{v_r} + \mathbf{w} \times \mathbf{w} \times \mathbf{r}]$ is composed by the Coriolis acceleration ($\mathbf{2w} \times \mathbf{v_r}$) and the centripetal acceleration ($\mathbf{w} \times \mathbf{w} \times \mathbf{r}$). The stress tensor $\boldsymbol{\tau}_r$ keeps its mathematical structure, but it uses relative velocities.

SM models the rotation of the grid by adding a source term as a function of time in Eq. (8) allowing a relative movement of the adjacent grids among themselves. The SM equation is formulated for a scalar (ϕ) as follows:

$$\frac{\mathrm{d}}{\mathrm{d}t}\int_{\mathrm{V}}\rho\phi dV + \int_{\partial\mathrm{V}}\rho\phi\left(\mathbf{u}-\mathbf{u_g}\right)\cdot\mathrm{d}\mathbf{A} = \int_{\partial\mathrm{V}}D\nabla\phi\cdot\mathrm{d}\mathbf{A} + \int_{\mathrm{V}}S_\phi dV \tag{24}$$

where V is the control volume, D is the diffusion coefficient, S_ϕ is a source term, $\mathbf{u}$ is the flow velocity vector, $\mathbf{u_g}$ is the velocity of the moving grid, and ∂V is the control volume interface.

A third manner to model the movement of mechanical parts is through the boundaries of the walls; this approximation was named tangential rotation (ROT) and holds true only for viscous flows (non-slip condition).

8. Numerical method

Two numerical solvers can be selected in Fluent®. The first is a pressure-based solver that was initially developed for high-speed incompressible flow. The second is a density-based that was developed for high-speed compressible flow. Regardless of the solver being used, the velocity field is calculated from the momentum equations [19]. The general solution algorithm can be divided in three stages:

1. Generation of the discrete volumes (computational grid).
2. Discretization of the conservation equations.
3. Linearization of the discretized equations and solution of the resulting system.

The pressure-based solver is established from the pressure-correction equation obtained from the momentum and continuity equations. Convergence is reached when the estimated velocity field satisfies the continuity condition:

$$\sum_{f}^{N_{faces}} J_f A_f = 0 \tag{25}$$

where J_f is the mass flux and A_f is the surface area of face "f". In the pressure-based methods, there are segregated algorithms based on corrector-predictor approximations (e.g. SIMPLE, SIMPLEC and PISO). SIMPLE algorithm or semi-implicit method for pressure-linked equations satisfies Eq. (25) by correcting the flux J_f through J'_f and by the corrected pressure p'. The algorithm postulates that J'_f follows Eq. (26) [19]. J^*_f is calculated by using the pressure field p^*.

$$J_f^{'} = d_f\left(p_{c0}^{'} - p_{c1}^{'}\right) \tag{26}$$

$$J_f = J_f^{*} + J_f^{'} \tag{27}$$

$$J_f = J_f^{*} + d_f\left(p_{c0}^{'} - p_{c1}^{'}\right) \tag{28}$$

9. Methodology

The following materials were obtained from Sigma Aldrich (Munich, Germany) and were used without any further purification: AAm (99.8%) and AMPS (99%). Ammonium persulfate or APS (98%) was obtained from Tecsiquim (State of Mexico, Mexico). AMPSNa preparation is reported elsewhere [21]. The molar ratio of the monomers (1:1) was constant with a total initial concentration of 10.6% wt. The initial concentration of APS was kept constant at 0.5% wt. Polymerization progress was followed in an Anton Paar® MCR 301 Rheometer with a concentric cylinder geometry (CC27/CX) coated with polytetrafluoroethylene. A batch of reagents was prepared and then divided into seven samples that were polymerized at different shear rates as shown in **Table 1**.

Experiment	C1	C2	C3	C4	C5	C6	C7
Shear rate [s^{-1}]	10	30	60	90	120	150	200

Table 1. Set of AAm and AMPSNa copolymerization experiments at 60°C.

In relation to the CFD simulation, the geometry and the grid were constructed in Gambit®. The dimension of the geometry described the Parr® batch reactor used in the experimental work. Geometrically, the computational model is composed by a cylinder in whose interior a stirrer with rectangular impeller blades is located.

After designing the grid, sensitivity analysis was carried out to compare the velocity field magnitude in two grids with different cell sizes. The first grid (M_{200k}) contains 201,927 cells, while the second (M_{400k}) holds 482,312 cells. Pure water was used for both simulations.

Afterwards, Fluent® simulations were run to select a turbulence and stirring model. Experimental validation of the computational model was done by injecting 1 mL of 1 M sodium hydroxide solution (tracer). The response of the tracer was quantified with the multiparametric device OAKTON® PC 2700.

To correlate the shear rate and the stirrer speed in a batch stirred reactor, Eqs. (29) and (30) are used. This allows the comparison of stirring between the two systems used in this work, the reactor and the rheometer.

http://dx.doi.org/10.5772/64156

$$\dot{\gamma} = 0.107255 N^{1.4} \tag{29}$$

$$N = \left(\frac{\dot{\gamma}}{0.107255} \right)^{\frac{1}{1.4}} \tag{30}$$

where $\dot{\gamma}$ is the shear rate [s^{-1}] and N [rpm] is the stirrer speed. This relation was studied theoretically and experimentally by Sanchez, see [22]. The Re number was used to verify the turbulence.

$$Re = 117.39 \cdot N \tag{31}$$

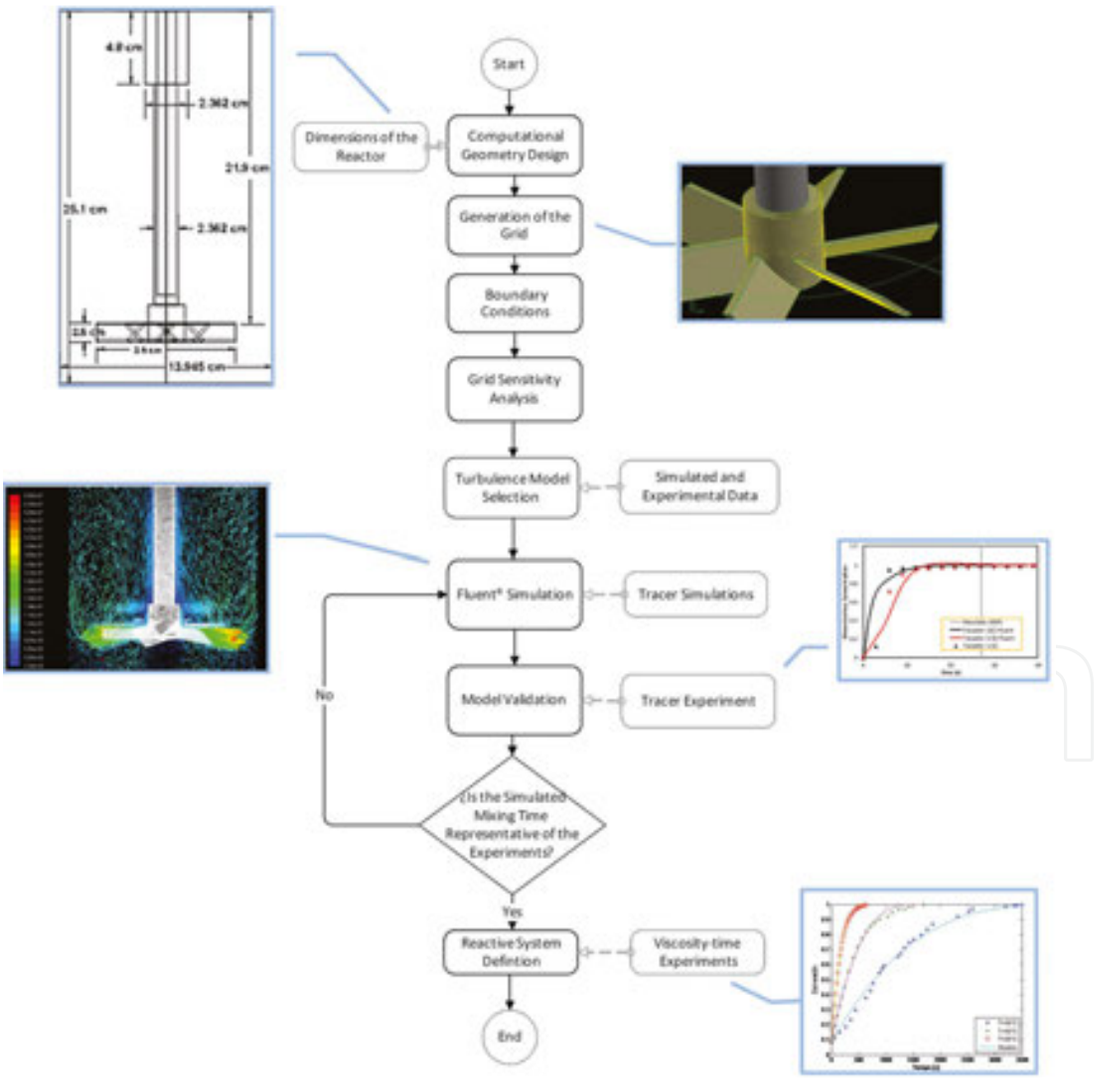

Figure 3. Work route for simulations of stirred tanks in Fluent®.

The number 117.39 was calculated for the reactor filled with liquid water (viscosity of 0.001 Pa·s and density of 998.2 kg/m^3) and by using the geometrical dimension of the system.

The methodology used for the simulations is presented in **Figure 3**. The diagram contains the experimental test used to validate the simulation model.

10. Kinetics of polymerization

For the synthetized copolymers of **Table 1** the experimental viscosity-time curves are presented in **Figure 4**, an adjustment of experimental data was done by using Eq. (4).

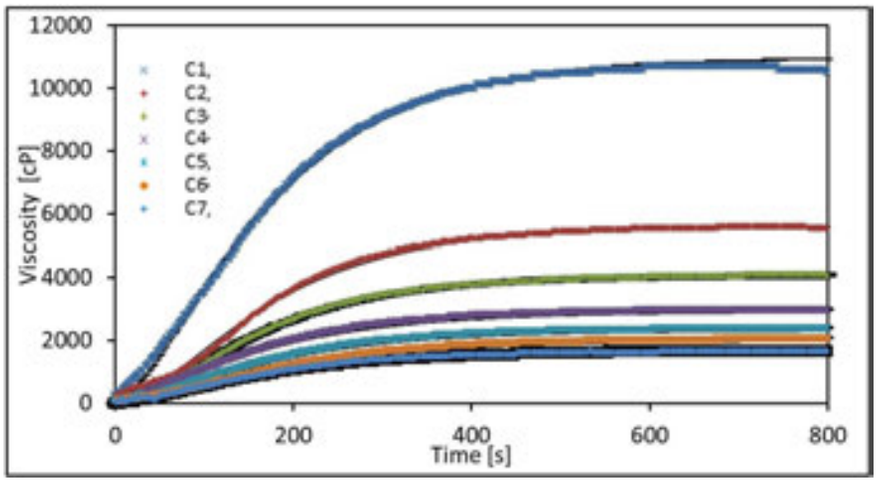

Figure 4. Viscosity-time data at 60°C and predicted data (–) from Eq. (4).

The numerical results of this regression are presented in **Table 2**.

Experiment	Shear rate [s^{-1}]	Stirrer speed [rpm]	k_v [s^{-1}]	$k_p/k_t^{1/2}$[$L^{1/2}mol^{-1/2}s^{-1/2}$]
C1	10	26	7.36×10^{-03}	0.00034
C2	30	56	7.87×10^{-03}	0.00075
C3	60	92	8.32×10^{-03}	0.00074
C4	90	123	7.21×10^{-03}	0.00374
C5	120	151	7.66×10^{-03}	0.00715
C6	150	177	7.03×10^{-03}	0.00535
C7	200	217	7.67×10^{-03}	0.01099

Table 2. Kinetic parameters obtained from experimental data.

It was found that $k_p / k_t^{1/2}$ is proportional to the shear rate used in the synthesis. k_d values are kept constant through all experiments, concluding that the initiation kinetics is independent of the shear rate. The copolymers were characterized to obtain a better understanding of the chemistry involved in the synthesis.

All copolymers were characterized by the following techniques: Fourier transform infrared spectroscopy (FTIR) in a Cary 600 Series spectrometer from Agilent®; differential scanning calorimetry (DSC) in an HP DSC 1 STAR® from Mettler Toledo® and rheology with a Physica MCR-301 Rheometer from Anton Paar®. The results of all these characterizations are presented in **Table 3**.

Experiment	Shear rate (s^{-1})	M_v(g/mol)	FTIR - F_2	DSC -T_g (°C)	DSC -T_f (°C)	T_g/T_f	$k_p/k_t^{1/2}$
C1	10	2.18E+05	50%	236.29	309.45	0.87	0.00034
C2	30	1.37E+05	43%	245.76	306.55	0.90	0.00075
C3	60	1.17E+05	49%	246.40	307.28	0.90	0.00074
C4	90	1.44E+05	45%	244.86	299.32	0.90	0.00374
C5	120	1.40E+05	48%	244.39	300.01	0.90	0.00715
C6	150	3.78E+05	47%	275.07	301.87	0.95	0.00535
C7	200	4.26E+05	42%	315.57	336.23	0.97	0.01099

Table 3. FTIR, DSC and rheological characterization of AAm-AMPSNa copolymers.

Based on the experimental results, the values of the M_v (molecular weight), T_g (glass transition temperature), and T_f (fusion temperature) increase according to the shear rate. M_v of polymers obtained under C6 and C7 conditions increased 281 and 317%, respectively, compared with C2. In all experiments, the AMPSNa molar composition of the copolymer chains was relatively constant (between 42 and 50%) according to the calculated F_2 parameter. This result was supported by the FTIR results.

Copolymers synthetized at 150 and 200 s^{-1} increased their T_g by 12% and 29%, respectively, considering a reference value of T_g=245°C. Increased values of T_g and T_f are consequences of both M_v [23] and stiffness of the chains. The latter is a consequence of the incorporation of sulfonate groups (e.g. AMPSNa) into the polymer [24].

11. Geometry, grid, and boundary conditions

The configuration of the grids for each stirring model (ROT, MRF, and SM) is shown in **Table 4**. A non-structured grid was adapted to generate tetrahedral and hybrid volumes (Tet/Hybrid).

Model	ROT	MRF	SM
Cells	381,352		201,927
Faces	783,158		439,109
Nodes	75,560		40,052
Volume elements	Mixed		
Elements in face	Triangular and quadrilaterals		
Volume (cm^3)	3757.353		3758.577
Fluid regions	1		2

Table 4. Grid parameters for ROT, MRF, and SM models.

The geometry generated in Gambit® is presented in **Figure 5**. Zone A was defined as the stirred region, while zone B as the stationary region.

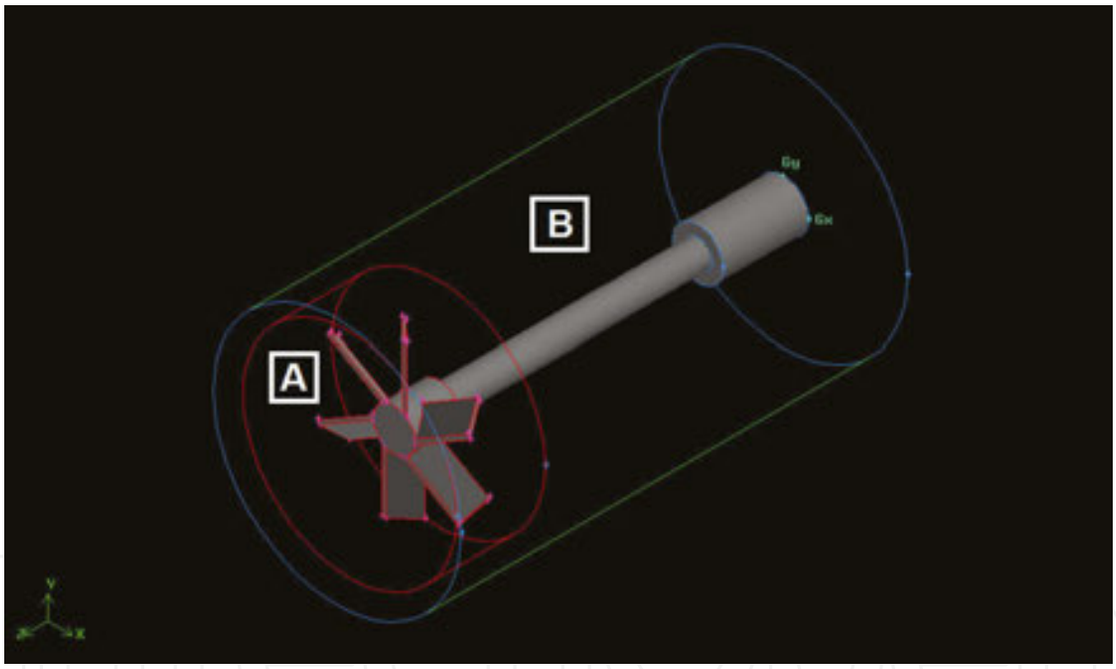

Figure 5. Isometric: stationary volume (A) and stirred volume (B).

The boundary conditions were defined as "walls" for the impeller and the reactor surfaces, which implies a no-slip condition. On the top face of the reactor, a zero-shear stress boundary condition was established, implying a free fluid movement. Region A was defined as "interior" during SM and MRF simulations. Only for SM an "interface" was defined in the boundary between the stirred and stationary volumes.

Using the original geometry, the effect of resized grid cells (M_{400k} and M_{200k}) on the mathematical simulation was analyzed through the velocity variation over a defined position within the reactor; such results are presented in **Figure 6**.

http://dx.doi.org/10.5772/64156

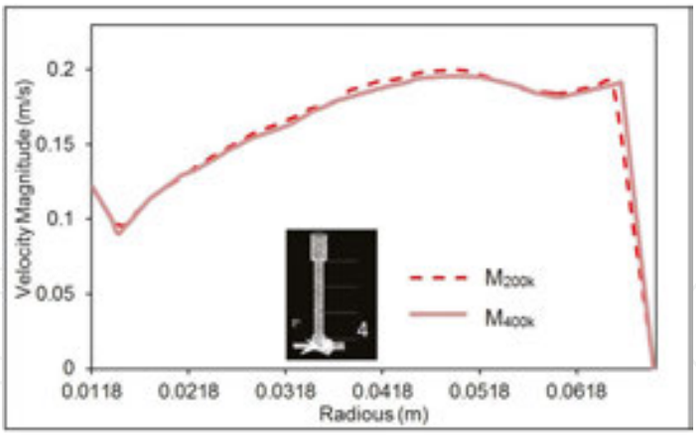

Figure 6. Radial velocity comparison between grids M_{400k} and M_{200k}.

12. Turbulence and stirring model selection

Standard, RNG and realizable k-ϵ were compared in terms of the convergence time. Global residual tolerances for all variables (velocity, continuity, k-ϵ) were kept constant at 1×10^{-3}. Realizable k-ϵ was selected due to its reduced convergence time (1305 iterations), this being compatible with the literature recommendation for high-velocity rotational flows [25, 26].

Various simulations with liquid water were performed at 100 rpm (Re=11,739) to select a stirring model (ROT, MRF, or SM). All simulations were run using a 3D no-stationary solver. Cross-sections, as shown in **Figure 11**, were used to visualize velocity profiles in the stirred tank. **Figures 7–9** show a typical velocity behavior of stirred tanks: a mixing zone in the upper section, high velocity gradients close to the moving blades, and a dead recirculation zone below the impeller. The mathematical model was validated by comparing the mixing time obtained against experimental data.

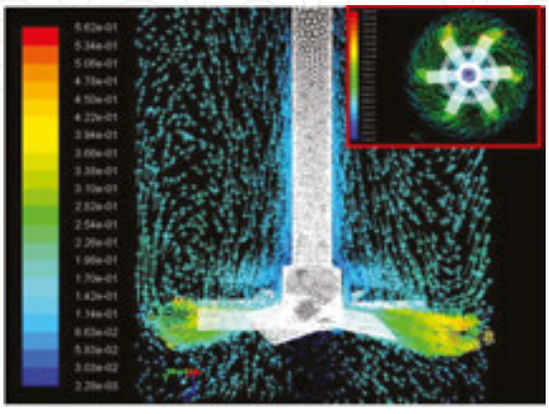

Figure 7. MRF, colored vectors by velocity magnitude in m/s (Scale/Omission relation of 50/1).

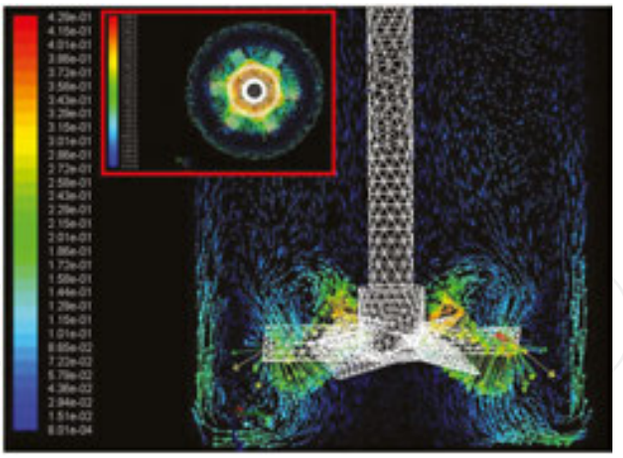

Figure 8. SM, colored vectors by velocity magnitude in m/s (Scale/Omission relation of 50/1).

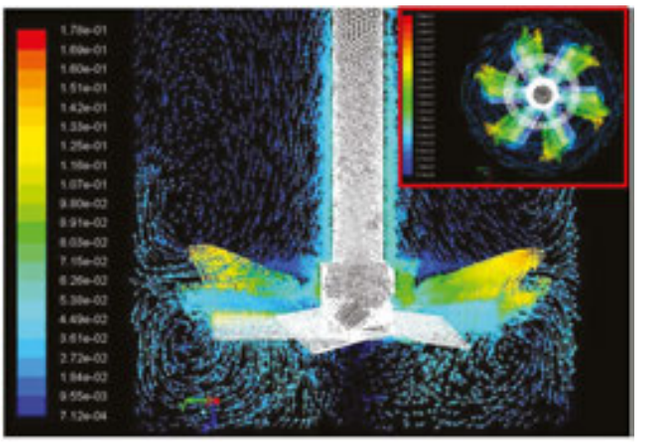

Figure 9. ROT, colored vectors by velocity magnitude in m/s (Scale/Omission relation of 50/1).

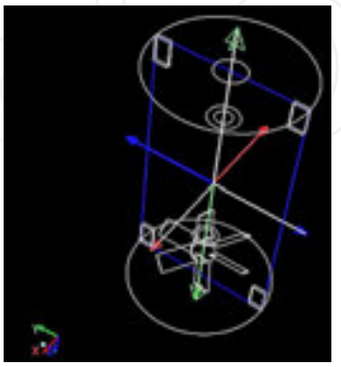

Figure 10. Cross-section for analysis of simulated data.

The graphics presented in **Figures 7–9** were taken from the cross-section defined in **Figures 10** and **11**. **Figures 7–9** show the velocity profiles of MRF, SM, and ROT models. The color

http://dx.doi.org/10.5772/64156

scale indicates the magnitude of each vector view from two planes: Y-Z and X-Y. All images enclosed in red squares are radial cross-sections near the blades.

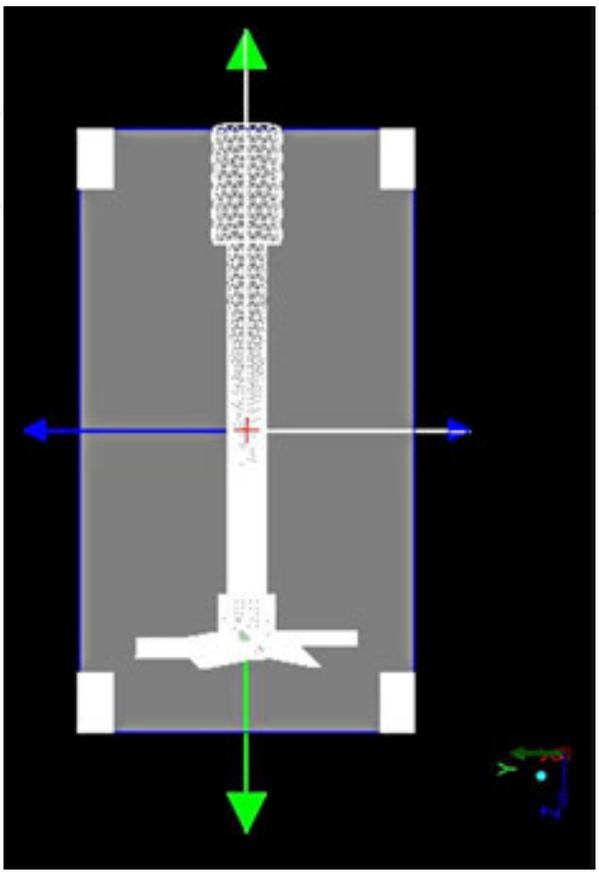

Figure 11. Cross-section defined in the Y-Z plane.

13. Tracer analysis in Fluent®

Tracer simulations were developed considering an unsteady state, using as initial condition, the data obtained at the stationary state solution (t=0). The stirrer speed was set at 100 rpm using liquid water and tracer as materials. Initial injection positions are shown in **Figure 12**. This configuration was used in all tracer simulations. Monitors were defined as spheres with a radius of 0.8 cm and were used to track the tracer concentration in a specific region (**Figure 13**).

Each monitor registers a mass fraction of tracer every 0.55 s. Results for all simulations are presented in dimensionless concentration.

Asymptotic behavior of the tracer concentration is a criterion to define the mixing time. Tracer curves for each model are shown in **Figures 14–16**.

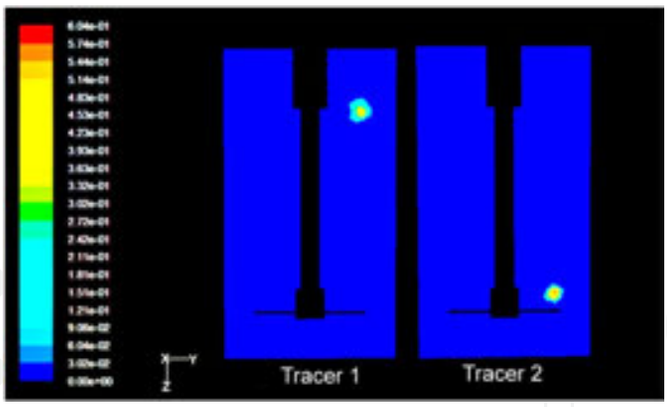

Figure 12. Tracer injection zones. Tracer 1 in (0, 4, 5) cm and Tracer 2 in (0, 4, 20) cm.

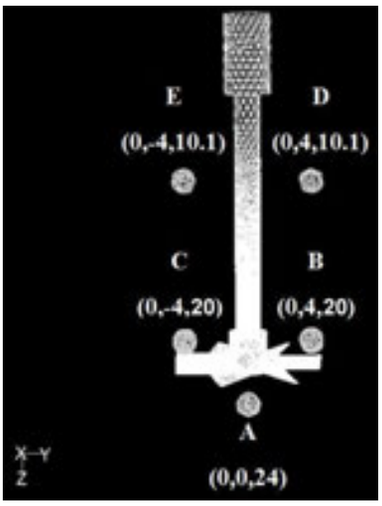

Figure 13. Spherical monitors and their spatial location.

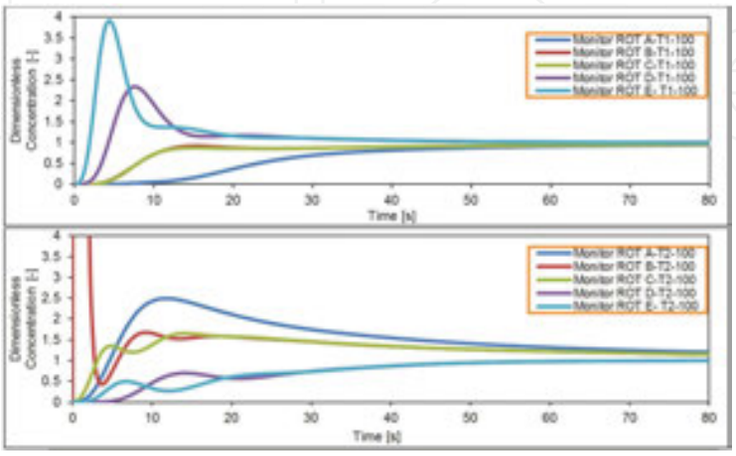

Figure 14. ROT tracer evolution curves after injection in regions 1 and 2.

http://dx.doi.org/10.5772/64156

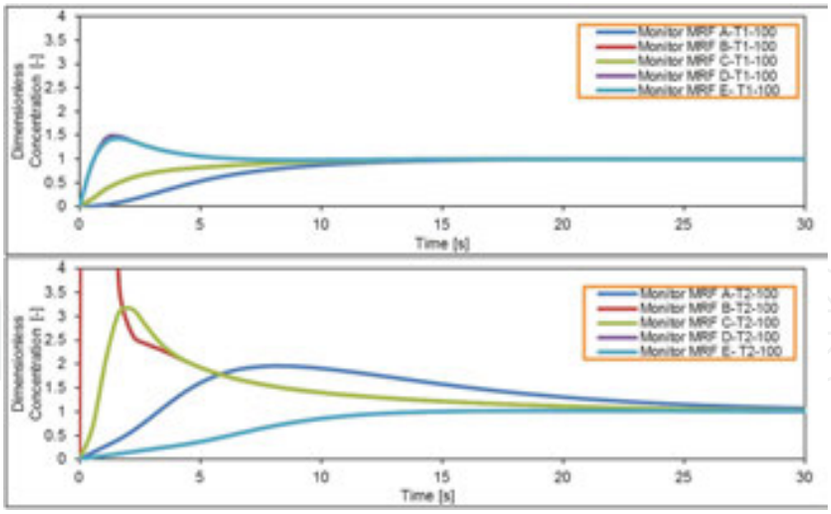

Figure 15. MRF tracer evolution curves after injection in regions 1 and 2.

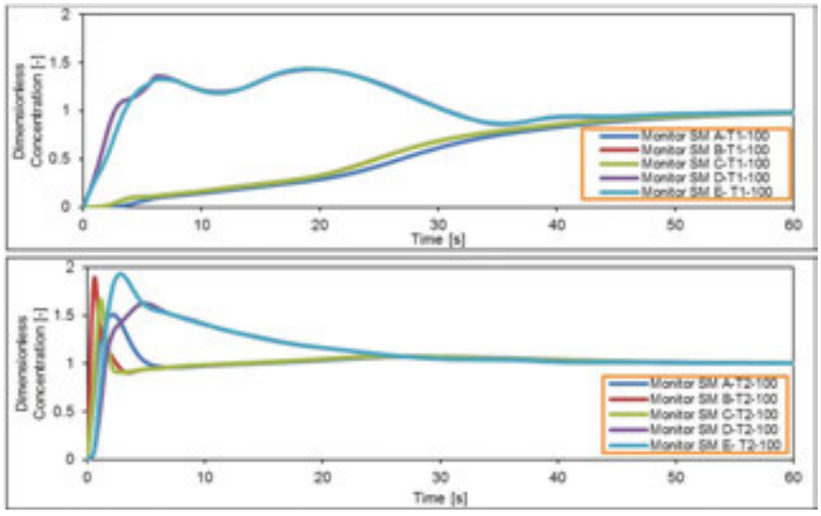

Figure 16. SM tracer evolution curves after injection in regions 1 and 2.

Mixing time of ROT simulations diverges drastically between injections. Tracer 1 curves start to become asymptotic at 80 s, while there is no clear tendency when the injection is made in region 2.

Results from **Figure 16** show a significant tracer concentration variation above 30 s. SM predicts that mixing time of all monitors is beyond 80 s.

SM tracer curves of **Figure 16** differ qualitatively and quantitatively from curves obtained in **Figures 14** and **15** (ROT and MRF). In general, the monitored tracer behavior is in agreement with the velocity field of a stirred tank.

Concentration contours are presented in **Table 5** for tracer 1 and 2. Mixing profiles are shown on a radial cross-section over the X-Y plane.

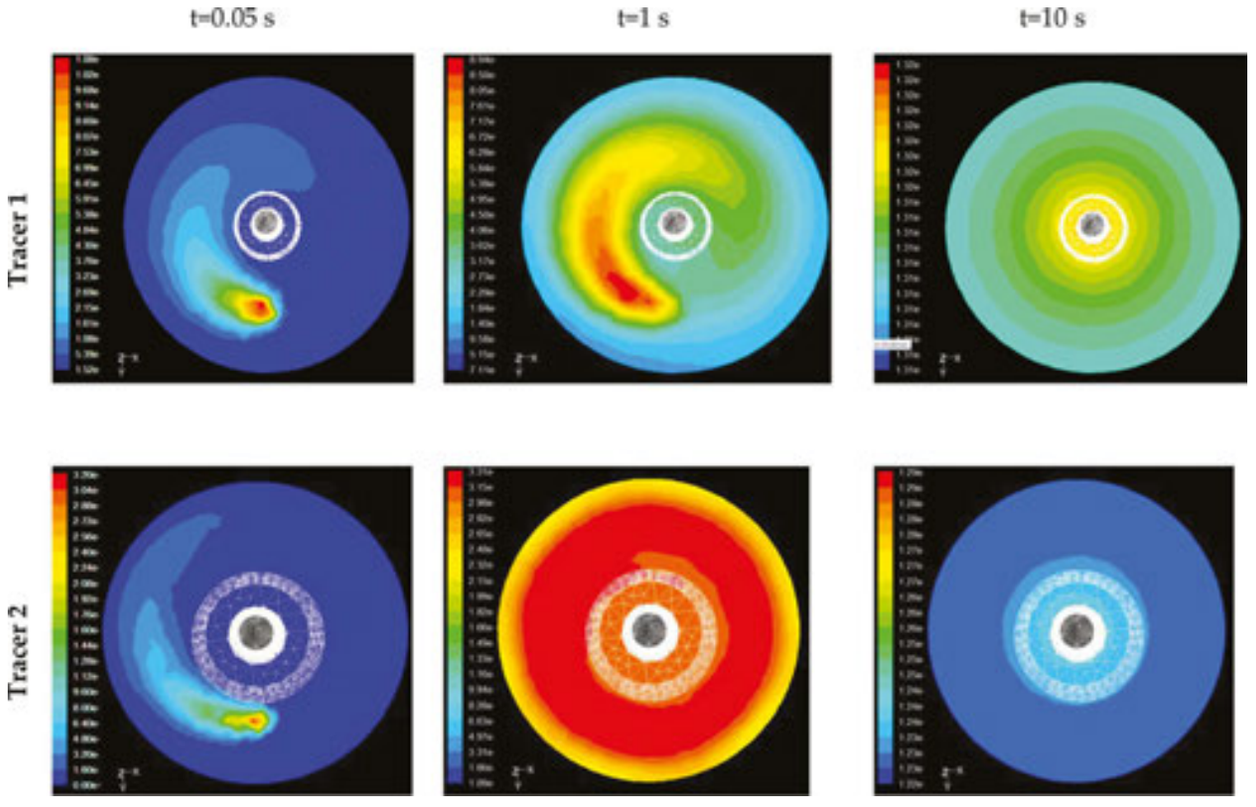

Table 5. Mass fraction of tracer dispersion at different times.

14. Validation of the computational model

The experimental mixing curves for Monitor C (Tracer 1) and E (Tracer 2) were obtained from pH data plots against time. Experimental and simulation data are compared in **Figure 17**.

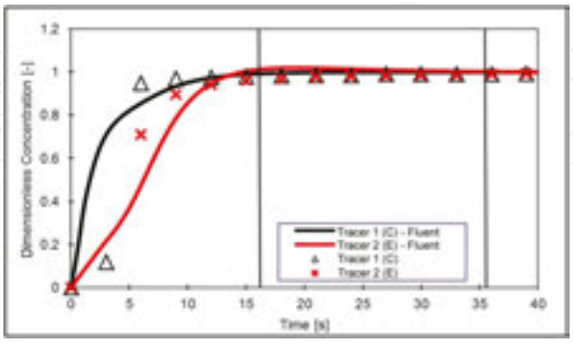

Figure 17. Comparison of experimental data (Δ,×) and numerically (—) obtained solutions.

Simulated curves in **Figure 17** were obtained at a stirrer speed of 100 rpm with liquid water, using MRF and realizable k-ϵ as working models. The injections were made in the regions established in **Figure 12**.

The mixing time for tracer 1 has a value of 15.4 s and for tracer 2, a total of 35.8 s (**Figures 18** and **19**). The criterion used to define the mixing time was the standard deviation of the concentration data registered in all monitors [26].

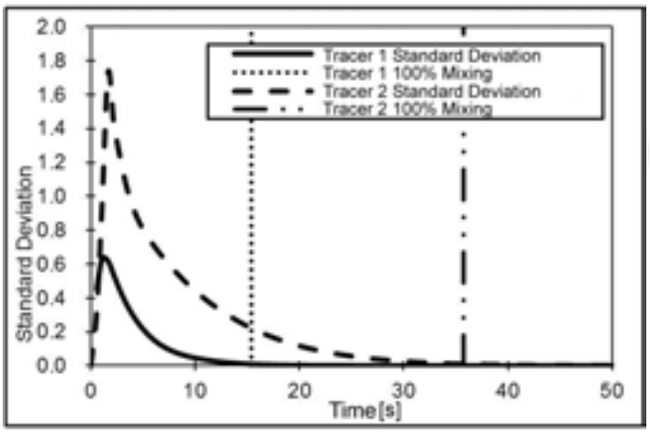

Figure 18. Standard deviation of data from MRF model at 100 rpm.

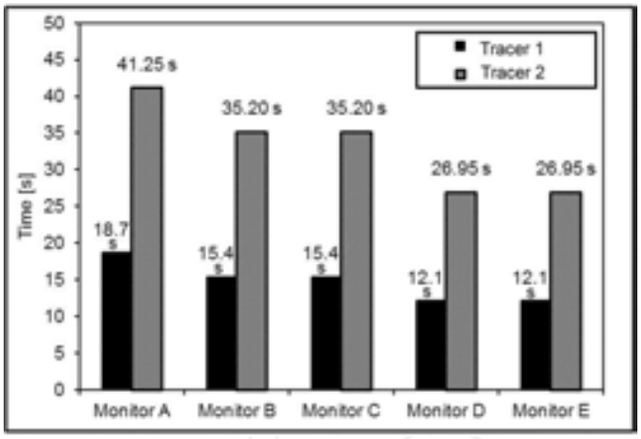

Figure 19. Mixing times of tracer 1 and tracer 2 (all monitors).

The experimental and numerical mixing times are shown in **Table 6**. The mixing time in Monitor C differs from the experimental value by 5 seconds, while Monitor E differs from it by 0.1 seconds. The resemblance between Monitors B-C and D-E is due to their spatial position.

Monitor	Tracer 1 (C)	Tracer 2 (E)
Experimental	21 s	27 s
Simulated	15.4 s	26.9 s
Global simulated	15.4 s	35.8 s

Table 6. Simulated and experimental mixing times for tracer 1 and 2.

The injection zone 1 (Tracer 1) allows a lower mixing time compared with the injection zone 2. However, mixing times of Monitors C and E are less sensitive to changes in stirrer speed.

The SM and ROT stirring models were discarded because the calculated mixing time does not correspond to the experimental data, as seen in **Figures 20** and **21**. Experimental mixing time is well fitted by MRF calculations.

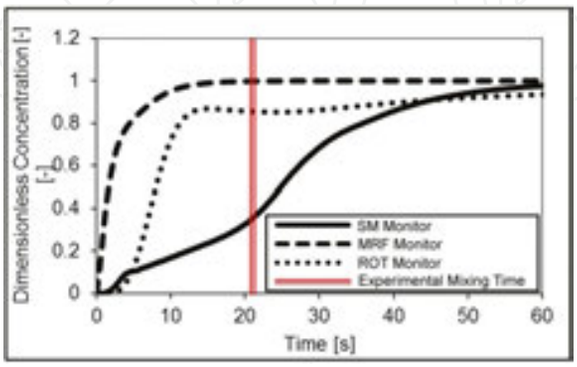

Figure 20. Tracer 1 curves, Monitor C (100 rpm) with 3 different models: MRF, SM, and ROT.

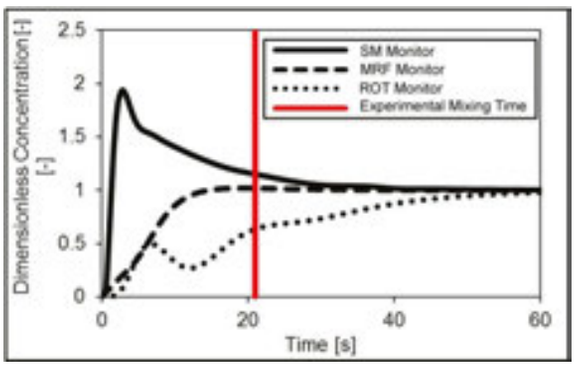

Figure 21. Tracer 2 curves, Monitor E (100 rpm) with 3 different models: MRF, SM, and ROT.

15. Effect of the stirring speed

Once MRF model was selected, a stirring speed swept from 100 to 300 rpm was done. Monitor C mixing time presents minor variations between 100 to 200 rpm; however, at 300 rpm the mixing time is drastically reduced (**Figure 22**). In contrast, in Monitor E the mixing time is reduced by increasing the stirring speed. An increase in the stirring speed leads to a reduced mixing time, allowing better contact among chemical species. Nevertheless, in the case of polymerization, a high stirring speed (above 300 rpm) can produce mechanical degradation of the formed chains.

http://dx.doi.org/10.5772/64156

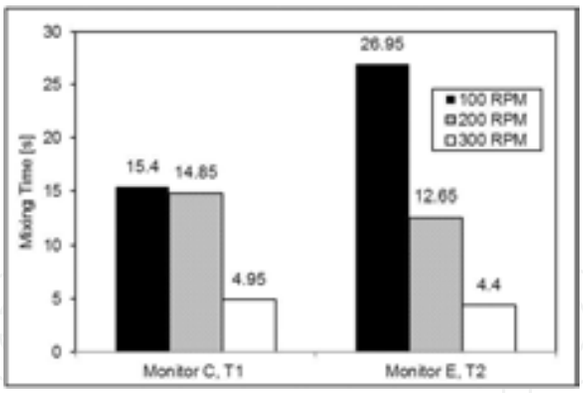

Figure 22. MRF simulated mixing times at 100, 200 and 300 rpm.

16. Conclusions

Chemical product design requires the development of standardized procedures to ensure reproducibility and quality of the synthetized product. If this is possible, then the impact of any experimental variation on the product properties can be properly analyzed and eventually, the optimization of the designed product can be reached.

To set up a procedure for the synthesis of an AAm-AMPSNa copolymer in a batch reactor, we have used CFD-simulations and rheokinetics. These tools were used to research the relationship between the polymerization reaction kinetics and the mixing process.

The AAm-AMPSNa copolymer properties (M_v, T_g and $k_p/k_t^{1/2}$) increase according to the shear rate (better mixing) in the synthesis. Specifically, the molecular weight of the polymer synthetized at the highest stirring speed (C7) increases up to 317% with respect to the lowest stirring speed in the stirred tank (C2), showing a direct relation between the mixing stirring times and the chemical kinetics.

MRF and realizable k-ϵ satisfactorily model the mixing process in the stirred tank. The tracer curves obtained numerically from CFD were experimentally validated using a 1 M NaOH tracer. The simulated mixing time differs by 0.4% with regard to the experimental value of Monitor E (Tracer 2).

According to the tracer analysis and the rheokinetics of the polymerization, it is recommended that reagents be injected (e.g. initiators or REDOX pairs) in the region defined as "Tracer 1," operating the reactor at 217 rpm (200 s^{-1}) and controlling the temperature at 60°C.

To give continuity to this work, we suggest to include the rheokinetics model in the transport phenomena equations, to consider rheology progression and its effect on the flow pattern, as a consequence of the growing polymer chains.

Acknowledgements

We gratefully acknowledge financial support of this investigation from "Fondo Sectorial CONACyT-SENER Hidrocarburos" under grant #0185183, "Proceso de Recuperación Mejorada con la Tecnología de Inyección de Químicos (ASP) con Aplicación Mediante Prueba Piloto en el Campo Poza Rica", and we sincerely thank the USIP from Facultad de Química, UNAM for the support. Finally, we appreciate the helpful suggestions of Ada Galena Barragán Aroche, for the grammar review on this manuscript.

Author details

Gerardo M. Pineda-Torres, Cecilia Durán-Valencia, Fernando Barragán-Aroche and Simon López-Ramírez*

*Address all correspondence to: simon.lopez.ramirez@gmail.com.

USIP, Chemistry Faculty, National Autonomous University of Mexico, Mexico City, Mexico

References

[1] Froment, G., Bischoff, K. Chemical Reactor Analysis and Design. New Jersey: John Wiley & Sons, Inc; 1979. 765 p.

[2] Ranade, V. Computational Flow Modelling for Chemical Reactor Engineering. Pune: Academic Press; 2002. 452 p.

[3] Meyer, T., Keurentjes, J. Handbook of Polymer Reaction Engineering. Lausanne: Wiley-VCH; 2005. 1102 p.

[4] Odian, G. Principles of Polymerization. 4th ed. New Jersey: John Wiley & Sons; 2004. 812 p.

[5] Harris, C., Roekaets, F., Rosendal, F. Computational fluid dynamics for chemical reactor engineering. Chemical Engineering Science. 1996; 51: 1569–1594.

[6] Patel, H., Ein-Mozaffari, F., Ramdhane, D. CFD analysis of mixing in thermal polymerization of styrene. Computers and Chemical Engineering. 2010; 34: 421–429.

[7] Bird, R., Stewart, W., Lightfoot, E. Transport Phenomena. New Jersey: John Wiley & Sons, Inc; 2002. 897 p.

[8] Levenspiel, O. Tracer Technology Modelling the Flow of Fluids. Berlin: Springer; 2012.137 p.

[9] Post, T. Understand the Real World of Mixing [Internet]. 2010. Available from: http://www.postmixing.com/publications/100315ceparticle.pdf [Accessed: 2016-03-01]

[10] López-Ramírez, S., Barreto, J. de J., Vite-Martínez, P., Romero-Serrano, J. A., Durán-Valencia, C. Physical and mathematical determination of the influence of input temperature changes on the molten steel flow characteristics in slab tundishes. Metallurgical and Materials Transactions B. 2004; 35B: 957–966

[11] Wever, D., Picchioni, F., Broekhuis, A. Polymers for enhanced oil recovery: a paradigm for structure-property relationship in aqueous solution. Progress in Polymer Science. 2011; 36: 1558–1628.

[12] Durán-Valencia, C., Bai, B., Reyes, H., Fajardo-López, R., Barragán-Aroche, F., López-Ramírez, S. Development of enhanced nanocomposite preformed particle gels for conformance control in high-temperature and high-salinity oil reservoirs. Polymer Journal. 2014; 46: 277–284.

[13] Barnes, H., Hutton, J., Walters, K. An Introduction to Rheology. Netherlands: Elsevier Science Publishers B.V.; 1989. 199 p.

[14] Malkin, A., Kulichikhin, S. Rheokinetics Rheological Transformations in Synthesis and Reactions of Oligomers and Polymers. Moscow: Wiley-VCH; 1996. 326 p.

[15] Brodke, R., Hershey, H. Transport Phenomena a Unified Approach. Ohio: McGraw-Hill; 1988. 847 p.

[16] Wendt, J. Computational Fluid Dynamics. Berlin: Springer-Verlag Berlin Heidelberg; 2009. 332 p.

[17] CFD-Online. History of CFD [Internet]. 2013. Available from: http://www.cfd-online.com/Wiki/History_of_CFD [Accessed: 2016-03-01]

[18] Soto, D. Análisis del mezclado en un reactor de polimerización de etileno. Bogotá. Universidad Nacional de Colombia; 2013.

[19] ANSYS Inc. Ansys Fluent Theory Guide [Internet]. [Updated: http://orange.engr.ucdavis.edu/Documentation12.0/120/FLUENT/flth.pdf]. Available from: 2010-03-01

[20] Santos, V., Brunet, L., Rolland, M. Numerical CFD simulation of a batch stirred tank reactor with stationary catalytic basket. Chemical Engineering Journal. 2012; 207–208: 596–606.

[21] Durmaz, S., Okay, O. Acrylamide/2-acrylamido-2-methylpropane sulfonic acid sodium salt-based hydrogels: synthesis and characterization. Polymer. 2000; 41: 3693–3704.

[22] Sánchez, J., Casas, J., Fernández, J. Shear rate in stirred tank and bubble column bioreactors. Chemical Engineering Journal. 2006; 124: 1–5.

[23] Chanda, M. Introduction to Polymer Science and Chemistry. Florida: Taylor & Francis; 2006. 640 p.

[24] Carraher, C. Polymer Chemistry. 6th ed. New York: Marcel Dekker, Inc.; 2003. 902 p.

[25] Marshall, E., & Bakker, A. Computational Fluid Mixing. Pennsylvania. ANSYS. Handbook of Mixing; 2001. TN144.

[26] Vite-Martínez, P., Durán-Valencia, C., Cruz-Maya J.A., Ramírez-López A., López-Ramírez S. Optimization of reagents injection in a stirred batch reactor by numerical simulation. Computers and Chemical Engineering. 2014; 60: 307–314.